RSC Advances

PAPER

View Article Online
View Journal | View Issue

Cite this: *RSC Adv.*, 2025, **15**, 7172

The effect of microstructure on mechanical and magnetic properties of FeCoNiAl$_{0.75}$Nb$_{0.25}$ high-entropy alloy†

Minh Duc Le,[a,b] Thanh Hung Nguyen,[b] Van Duong Nguyen,[b] Mai Khanh Pham[a] and Hong Hai Nguyen*[a]

Received 15th January 2025
Accepted 28th February 2025

DOI: 10.1039/d5ra00358j

rsc.li/rsc-advances

This work systematically investigated the relationship between the microstructure, and mechanical and magnetic properties of FeCoNiAl$_{0.75}$Nb$_{0.25}$ high-entropy alloy. Our results indicated that the microstructure of the alloy comprised a BCC solid solution phase along with a eutectic mixture of FCC and intermetallic phases. The application of heat treatment resulted in a significant evolution of the microstructure. The precipitation of the needle-like intermetallic phase occurred rapidly with increasing annealing temperature, reaching a maximum proportion at 825 °C, and decreased quickly upon further increase to 1000 °C. Correspondingly, the hardness and compressive yield strength of the alloy increased rapidly, attaining maximum values of approximately 600 HV and 2000 MPa, respectively. However, the precipitation adversely affected magnetic properties. The best values in the as-cast state for saturation magnetization, and coercive force are 0.67 T and 716 A m^{-1}, respectively, while the hardness remains 493 HV. Therefore, it is very suitable for magnetic parts requiring superior mechanical properties.

1. Introduction

High-entropy alloy (HEA) or multi-principal element alloy (MPEA) is a new alloy in materials science with many unique properties and broad application potential.[1] HEA exhibits superior properties such as high hardness and wear resistance,[2] the ability to maintain strength at high temperatures,[3,4] good ductility at low temperatures[5,6] and superplastic properties[7,8] when changing composition and microstructure. The majority of published HEA compositions are based on transition metals such as Co, Cr, Fe, and Ni, and enriched with elements such as Al, Cu, Mn, V, Nb, Ti, and Mo.[1,9–21] Nb is one of the alloying elements that can significantly influence the properties of FeCoNi-based high-entropy alloys. The microstructure of AlCoCrFeNb$_x$Ni HEA consists of two phases: BCC solid solution phase and Laves phase (CoCr)Nb type. As the Nb content increases, the microstructure of the alloy transitions from hypoeutectic to hypereutectic. Correspondingly, both Vickers hardness and compressive yield strength exhibit a nearly linear increase.[22] The AlCrFeNiCu alloy exhibits a two-phase structure with dendritic morphology. The addition of Nb facilitates the formation of fine eutectic structures, altering the grain morphology from cylindrical to equiaxed. The hardness, wear resistance, and compressive strength of the alloy improve with increased Nb content.[23] Additionally, the yield strength of (CoCrFeMnNi)$_{100-x}$Nb$_x$ ($x = 0, 4, 8, 12, 16$) HEA increased quite rapidly from 202 to 1010 MPa. However, when increasing the Nb content, the fracture strain decreased very quickly from 60% to 12%.[24] The microstructure of the CoCrFeNb$_x$Ni ($x > 0$) HEAs changes significantly as x increases,[25] from single-phase FCC solid solution structure to hypoeutectic, then to full eutectic and finally to a hypereutectic microstructure. As hardness and wear resistance increase, the plasticity decreases with increasing Nb content, due to the increase in the fraction of hard and brittle Laves phase. This shows the importance of Nb in the microstructure and properties of HEAs. Conversely, the current trend emphasizes reducing the number of elements and investigating new properties with high application potential, such as magnetic properties.[26] Li *et al.*[27] reported that increasing the molar fraction of Al to 0.7–1.0 in the FeCoNi-based alloys effectively reduces density while maintaining a relatively high saturation magnetization and low coercivity, consistent with a BCC structure. Additionally, the introduction of Nb enhances the stability of the BCC phase.[23] Specifically, incorporating 0.25 molar fraction of Nb maintains low density while preventing excessive brittleness in the alloy.[23] In this study, the FeCoNiAl$_{0.75}$Nb$_{0.25}$ alloy was designed to achieve a balance between reduced density and favorable magnetic properties. The relationship among the microstructure, mechanical properties, and magnetic properties of this alloy indicates its strong

---

[a] *School of Materials Science and Engineering, Hanoi University of Science and Technology, Hanoi, Vietnam. E-mail: hai.nguyenhong@hust.edu.vn*

[b] *Faculty of Mechanical Engineering, Le Quy Don Technical University, Hanoi, Vietnam*

† Electronic supplementary information (ESI) available. See DOI: **https://doi.org/10.1039/d5ra00358j**

potential as a soft magnetic material for applications such as generator rotors and coil cores. Notably, it exhibits superior mechanical properties compared to currently used alloys.

2. Experimental procedures

The FeCoNiAl$_{0.75}$Nb$_{0.25}$ alloy was synthesized using high-purity (>99.7%) elemental metals (Fe, Co, Ni, Al, Nb). The melting process was conducted in a vacuum induction furnace under a high-purity argon atmosphere, followed by casting into a water-cooled copper mold. The cast ingot has dimensions of 80 mm × 25 mm × 16 mm. Cut samples of size 5 mm × 5 mm × 5 mm were annealed at various temperatures of 600, 700, 825 and 1000 °C for 24 hours, followed by furnace cooling to room temperature. This prolonged annealing duration promotes the structural transformation from dendritic to equiaxed morphology, and facilitates the completion of the equilibrium precipitation. These samples denoted as HT-600, HT-700, HT-825 and HT-1000, respectively. Fig. 1 shows the fabrication process of the HEA samples. The XRD analysis was carried out using an Aeris diffractometer and Cu K$_\alpha$ radiation to determine the phase structure. The scanning speed is 3° min^{-1} with a scan range 20–80°.

The microstructure of the alloy was studied using an Axiovert A2M optical microscope, and secondary electron (SE) imaging in scanning electron microscopy (SEM) was utilized to analyze the surface morphology of the samples. The SEM images were acquired using a Jeol JSM-IT200 device at an accelerating voltage of 10 kV, with a working distance of 10 mm. The chemical composition of the ingot was analyzed using energy-dispersive spectroscopy (EDS), as listed in Table 1. It showing that the as-cast state composition is quite close to the nominal composition. For microstructural observation, specimens were ground to x2000 SiC paper, polished, and etched in aqua regia solution ($HNO_3 : HCl = 1 : 3$). Vickers hardness (HV3) was measured on a Wilson Wolpert machine under a load of 3 kg for 15 s. Each sample was measured five times to get the average value. The magnetization curves were measured at room temperature using a Lake Shore 7404 vibrating sample magnetometer (VSM). The specimens were cut to dimensions of 5 mm in width, 2 mm in thickness, and 5 mm in length using a wire electrical discharge machine.

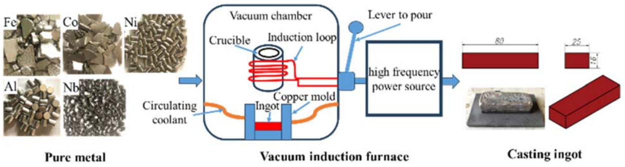

Fig. 1 Schematic diagram of the fabrication process.

Table 1 Composition of the as-cast FeCoNiAl$_{0.75}$Nb$_{0.25}$ alloy (wt%)

Element	Fe	Co	Ni	Al	Nb
Nominal composition	25.74	27.17	27.05	9.33	10.71
Actual composition	26.98	27.44	26.56	7.27	11.75

3. Results and discussion

3.1 Phase analysis

In Fig. 2a, the XRD patterns reveal that the as-cast alloy consists of a mixture of FCC, BCC, and intermetallic (IM) phases. The BCC phase, with a lattice parameter of $a = 0.2871$ nm, is enriched in FeCoNiAl,[22] while the FCC phase, characterized by a lattice parameter of $a = 0.3592$ nm, is predominantly FeCoNi-rich.[28] The IM phase is identified as the (Nb$_{0.5}$Al$_{0.5}$)Co$_2$ Laves phase, exhibiting a hexagonal close-packed (HCP) structure with lattice parameters $a = 0.4752$ nm and $c = 0.7746$ nm, as referenced in the PDF card. The diffraction pattern reveals that the BCC phase predominates, while the IM and FCC phases are present in smaller quantities. During heat treatment at 600 and 700 °C (Fig. 2b and c), the peak of the BCC phase is notably reduced, whereas the peaks of the FCC and IM phases are enhanced. When heat treatment is carried out at 825 °C, the IM phase reaches its peak, and the proportion of the BCC phase increases once more (Fig. 2d). In particular, at the BCC phase positions coexist two adjacent diffraction peaks. An additional peak corresponding to the IM phase appears as shown in Fig. 2e, this phase can be Co$_2$Nb Laves phase with a cubic lattice structure according to PDF Card. The lattice parameters are $a = 0.6759$ nm. When the temperature reaches to 1000 °C, the proportion of the IM phase decreases clearly and mainly Co$_2$Nb phase. We concluded that Al is depleted in the IM phase with increasing annealing temperature. The intensity of the FCC phase increases gradually with annealing temperature, then remains nearly constant. This is related with the high entropy effect that significantly lowers the Gibbs free energy of the system,[1] which more easily yields the formation of solid solutions during solidification rather than ordered compounds, especially at the high temperature, and leads to the total number of phases well below the maximum equilibrium number allowed by the Gibbs phase rule.[1]

Several related research suggested that the formation of phases in high-entropy alloys can be predicted by thermodynamic parameters,[21,29,30] including the difference in atomic size (δ), the mixing enthalpy (ΔH_{mix}), the mixing entropy (ΔS_{mix}), valence electron concentration (VEC), and Ω criterion:

$$\delta = \sqrt{\sum_{i=1}^{n} c_i (1 - r_i/\bar{r})^2} \tag{1}$$

$$\Delta H_{\text{mix}} = 4 \sum_{i=1, i \neq j}^{n} \Delta H_{ij}^{\text{mix}} c_i c_j \tag{2}$$

$$\Delta S_{\text{mix}} = -R \sum_{i=1}^{n} (c_i \ln c_i) \tag{3}$$

$$\text{VEC} = \sum_{i=1}^{n} c_i (\text{VEC})_i \tag{4}$$

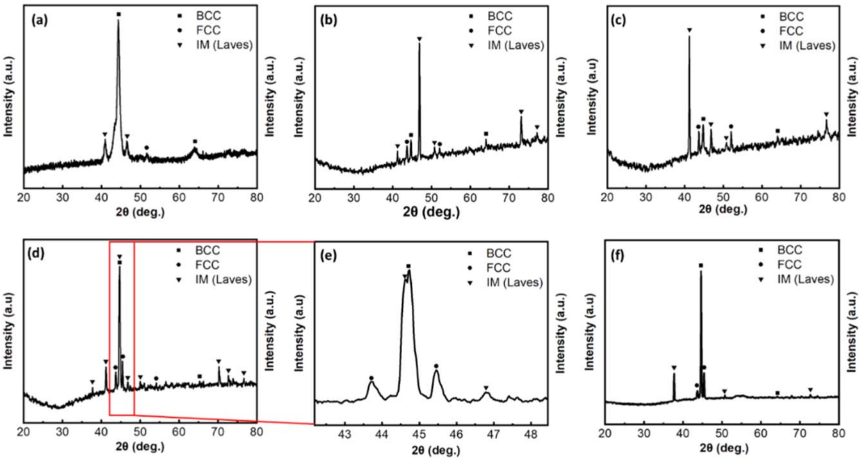

Fig. 2 The XRD patterns of the alloy: (a) As-cast, (b) HT-600, (c) HT-700, (d) HT-825, (e) enlargement of $2\theta = 42–48.5°$ region in HT-825 sample and (f) HT-1000.

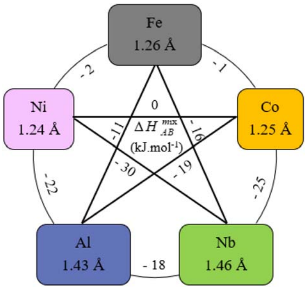

Fig. 3 Values of ΔH^{mix}_{AB},[31] atomic radius of elements[32] in FeCoNiAlNb HEA.

$$\Omega = \frac{T_m \Delta S_{mix}}{|\Delta H_{mix}|} \tag{5}$$

where $\bar{r} = \sum_{i=1}^{n} c_i r_i$, r_i is the Goldschmidt atomic radius of the ith element, as shown in Fig. 3. c_i is the molar ratio and ΔH_{ij}^{mix} is the mixing enthalpy between the ith and jth elements, T_m is the average melting temperature, $(\mathrm{VEC})_i$ valence electron concentration of element i and $R = 8.314$ J K^{-1} mol^{-1} is the gas constant.

According to the Hume–Ruthery rule, the difference in atomic size (δ) and the enthalpy of mixing (ΔH_{mix}) are the two factors that solid solution phase stability in HEA. Guo *et al.*[32] predicted that the easily formation of a solid solution phase corresponds to the region $- 22$ kJ mol^{-1} $\leq \Delta H_{mix} \leq 7$ kJmol^{-1} and $0 < \delta < 8.5\%$. On the other hand, M. Enoki et al.[33] found that -20 kJ mol^{-1} $\leq \Delta H_{mix} \leq -10$ kJ mol^{-1} can form additional IM phases in FeCoNi-based alloys. According to these two parameters, the alloy exhibits the values of $- 15.78$ kJ mol^{-1} and 6.3%, respectively, indicating a tendency to form a mixed phase including solid solution and IM phases.[21,33] Moreover, the other parameters for forming a solid solution have been established: $11 \leq \Delta S_{mix} \leq 19.5$ (J K mol^{-1}) and $\Omega \geq 1.1$.[29] These precise conditions ensure that the solid solution phase is preferentially formed first, followed by the IM phase. Additionally, it should be noted that HEA with a VEC ≥ 8.0 tend to form an FCC phase, whereas a BCC phase is more likely to form when the VEC ≤ 6.87.[30] Within the range of $6.87 \leq$ VEC < 8.0,[30] the FCC/BCC mixture phases are stable.

For the as-cast FeCoNiAl$_{0.75}$Nb$_{0.25}$ alloy, the values of these parameters after calculation are listed in Table 2. It can be seen that the values of parameters were consistent with the formation rules of solid solution. With the result from XRD pattern, the phase of this HEA mainly consists of the BCC, and a small portion of the FCC and IM phases.

3.2 The as-cast microstructure

The as-cast microstructure of the FeCoNiAl$_{0.75}$Nb$_{0.25}$ alloy is illustrated in Fig. 4 and S1 of the ESI.† It can be seen that the microstructure is characterized by coarse dendritic phases measuring up to few hundred μm in length (λ_1), as depicted in Fig. 4a. The distance between the secondary dendrites (λ_2) is measured up to ~11 μm, as shown in Fig. 4b. Additionally, the inter-dendritic phase is fine, the proportion of this phase is about 23%, as displayed in Fig. 4c.

The SEM image of as-cast sample is depicted in Fig. 5. It reveals that the IM phase exhibits the morphology as a typical eutectic-like phase (Region B).[34] While the dendritic region

Table 2 Thermodynamic parameters of the alloy

ΔH_{mix}, kJ mol^{-1}	ΔS_{mix}, J K^{-1} mol^{-1}	δ, %	VEC	Ω	Phase in this work
−15.78	12.7	6.30	7.63	1.35	FCC + BCC + IM

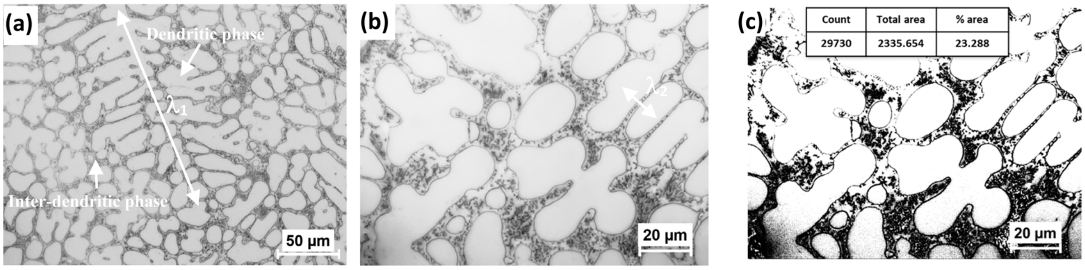

Fig. 4 (a and b) The as-cast microstructure (optical microscope images), and (c) the fraction of interdendritic phase was determined using ImageJ software.

(Region A) is a single-phase solid solution. The EDS analysis results of the regions are shown in Table 3. It shows that solid solution phase (Region A) is enriched in Ni and Al and depleted in Nb and Fe. The nature of such observation corresponds to the BCC phase, as Al and Ni promote the formation of this phase.[22] On the other hand, the eutectic phase (Region B) is rich in Fe, Co and Nb, but depleted in Al and Ni. The possible cause for this phenomenon is the relatively small atomic size of Ni (Fig. 3), which allows it to be readily dissolved into the supersaturated BCC solid solution during solidification, forming an interstitial solid solution. Moreover, Al and Ni have similar FCC lattice structures and considerable bonding energy due to their highly negative enthalpy of mixing (-22 kJ mol^{-1} for the Al–Ni atomic pair). Concerning Nb, it has the largest atomic size (0.146 nm) in this alloy system as well as very negative enthalpies of mixing with other alloying elements (Fig. 3), which are not favorable to form the solution with them, that is why Nb conversely enhances the tendency to segregate to form the ordered Nb-rich Laves phases.[22] Based on the EDS analysis results in Table 4 and XRD pattern, the eutectic plates are rich in Co and Nb, suggesting they likely belong to the (AlNb)Co Laves phase. Meanwhile, the remaining phase of the eutectic structure is rich in Fe, Co, and Ni, but deplete in Al, corresponding to the FCC phase.[35] Based on the above analysis, we can identify and label the phases, as described in Fig. 5b.

Table 3 The results of the EDS analysis (wt%)

	Fe	Co	Ni	Al	Nb
Region A (BCC phase)	24.33	27.38	33.33	10.65	4.29
Region B (eutectic phase)	29.00	28.00	17.64	3.64	21.71

3.3 The microstructure of annealed alloy

Fig. 6 presents the SEM image of the FeCoNiAl$_{0.75}$Nb$_{0.25}$ alloy sample after annealing, with optical imaging in Fig. S2 of the ESI† used as a supplementary technique to identify the present phases. Following annealing at 600 °C, the microstructure almost retains the as-cast form, although the dendritic phases become more uniform and equiaxial. The changes become more noticeable after annealing at 700 °C, where the eutectic phase thickens significantly, mainly due to an increase in the number of eutectic plates. This explains the observed increase in diffraction intensity for the IM phase and a corresponding decrease for the BCC phase. Meanwhile, the solid solution region precipitates numerous small, fine IM phases, each about a few hundred nanometers in size, and forms an interwoven needle-like shape (Fig. 6d) after annealing at 825 °C. The number of this phase decrease significantly when increasing the temperature to 1000 °C. Moreover, a shift and decrease in the peak intensity for the IM phase are observed as the annealing temperature increases from 700 to 825 °C (Fig. 2c and d). It is possible that the eutectic plates (IM phase) start to dissolve into the solid solution phases, leading to the morphology of this phase starting to plastic flow at grain boundaries and form deep grooves as shown in Fig. 6e. At higher temperatures (1050 °C), even for a much shorter holding time (one hour), the boundary can be softened, even partly remelted.

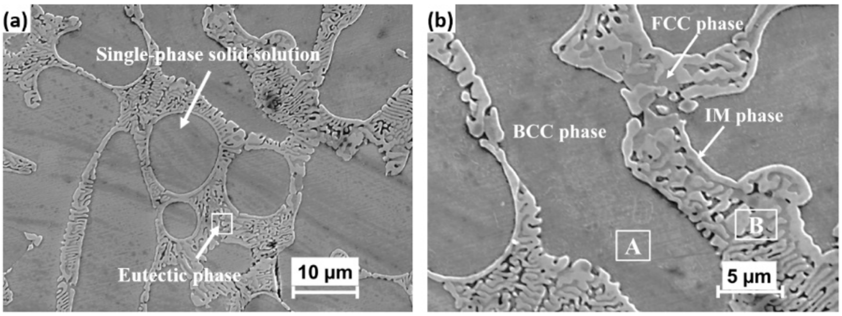

Fig. 5 The secondary electrons SEM images of as-cast sample.

Table 4 EDS analysis results of heat treatment samples[a]

		Chemical composition (wt%)				
Samples	Phase	Al	Fe	Co	Ni	Nb
HT-600	BCC phase	10.26	26.01	26.90	30.90	5.93
	Eutectic phase	2.90	23.39	25.82	20.55	27.33
	Eutectic plate (IM phase)	1.53	23.58	28.97	13.38	32.54
	Inter-eutectic plate (FCC phase)	3.98	30.33	28.26	32.32	5.11
HT-700	BCC phase	9.96	23.06	25.41	35.49	6.08
	Eutectic phase	3.85	24.75	26.66	24.73	20.02
	Eutectic plate (IM phase)	2.35	23.40	30.77	13.65	29.84
	Inter-eutectic plate (FCC phase)	3.83	30.43	29.49	31.16	5.09
HT-825	BCC phase	5.49	24.64	29.51	23.29	17.07
	Eutectic phase	0.56	20.13	29.51	15.59	34.11
	Precipitated phase	2.60	21.79	33.47	14.46	27.67
HT-1000	BCC phase	2.13	25.33	32.13	38.09	2.32
	Eutectic phase	0.92	23.44	31.04	13.01	31.58
	Precipitated phase	1.58	23.04	29.24	15.72	30.42

[a] An example of the EDS analysis position of the HT-700 sample is shown in Fig. S3.

The DSC analysis revealed that phase precipitation commenced at approximately 755 °C (Fig. 7), indicating that needle-shaped precipitated phases are likely to start forming within the BCC phase at this temperature. Additionally, two endothermic peaks were observed around 680–700 °C, which likely correspond to the dissolution of some non-equilibrium phases at these temperatures. This observation could account for the absence of phase precipitation when annealing at 700 °C and the subsequent decomposition of the eutectic phase as previously analyzed.

The EDS analysis results of heat treatment samples are summarized in Table 4. It can be seen that the BCC phase becomes increasingly deplete in Al, and rich in Ni and Co as the annealing temperature increases. That means there has been the diffusion of Al out of the BCC phase formed after casting. In particular, in sample HT-825, the Co and Nb contents increased significantly in this phase. This is likely due to the formation of the Co_2Nb intermetallic phase, as confirmed by XRD results.

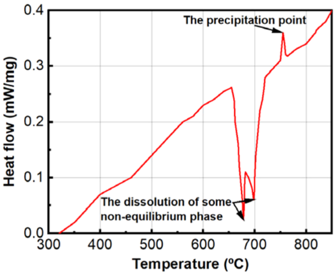

Fig. 7 The DSC curve of alloy.

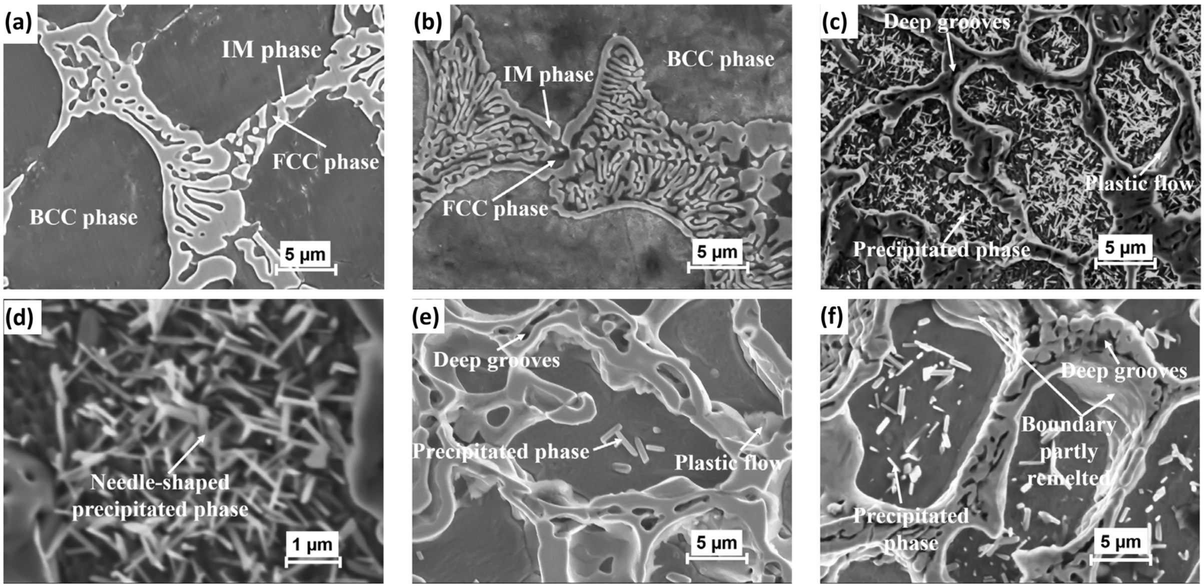

Fig. 6 The secondary electrons SEM images of the annealed alloy: (a) HT-600, (b) HT-700, (c and d) HT-825, (e) HT-1000, (f) HT-1050 with holding time of one hour.

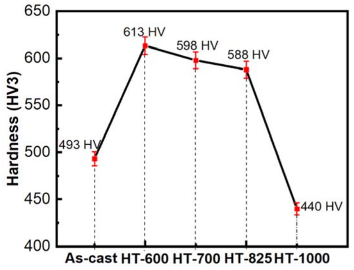

Fig. 8 The measured hardness of samples.

Table 5 The measured mechanical properties, including Vickers hardness (HV3, MPa) and compressive yield strength (σ_y, MPa) of alloy

Alloys	HV, MPa	σ_y, MPa	Ref.
$FeCoNiAl_{0.75}Nb_{0.25}$ as-cast	4832	1611	This work
$FeCoNiCrNb_{0.25}$ as-cast	2940	423	Jiang *et al.*[25]
AlCrFeNiCu+5 at% Nb as-cast	2695	1110	Malatji *et al.*[23]
$(FeCoNiCrMn)_{88}Nb_{12}$ as-cast	—	1010	Qin *et al.*[24]
$FeCoNiAl_{0.75}Nb_{0.25}$ HT-600	6007	2002	This work
$FeCoNiAl_{0.75}Nb_{0.25}$ HT-700	5860	1953	This work
FeCoNiAlMn HT-700	3558	1186	Yang *et al.*[40]
$FeCoNiAl_{0.75}Nb_{0.25}$ HT-825	5762	1921	This work
FeCoNiAlMn HT-800	3066	1022	Yang *et al.*[40]
$FeCoNiAl_{0.75}Nb_{0.25}$ HT-1000	4312	1437	This work
FeCoNiAlMn HT-1000	2994	998	Yang *et al.*[40]
FeCoNiCrMn HT-1000	1350	162	Salishchev *et al.*[20]
FeCoNiCrV HT-1000	5870	1435	Salishchev *et al.*[20]

The Nb content decreased rapidly with increasing temperature up to 1000 °C along with the decrease in the fraction of the precipitated phase in the BCC phase. The eutectic plate becomes richer in Al, and the remaining phase of the eutectic region maintains an almost constant content when heat-treated to 700 °C. Al tends to diffuse to the grain boundary and thicken this region when the temperature drops below 755 °C, as indicated by DSC data. Above this temperature, the Al and Ni contents rapidly decrease in the eutectic phase. According to the Gibbs phase rule, at higher temperatures, solid solutions are preferentially formed, leading to the dissolution of Al and Ni into the solid solution phase.

3.4 Mechanical and magnetic properties

As seen above, the microstructure of the alloy consists of a supersaturated solid solution and eutectic phases with a proportion high enough (23%), leading to very high hardness. The tensile specimens of the alloy exhibit brittle behavior, characterized by quite low elongation. Although the ductility of the alloy can be enhanced,[36,37] however the aim of the alloy is to achieve good magnetic properties while maintaining high strength so ductility is not a focus of this study. The hardness and yield strength of the alloy change significantly with heat treatment. As the annealing temperature approaches 825 °C, both properties increase sharply, stabilizing around 600 HV3 and 2000 MPa, respectively (Fig. 8 and Table 5). This enhancement can be attributed to the thickening of the eutectic phase (a non-equilibrium phase) in conjunction with the precipitation process within the matrix. However, at 825 °C, the decomposition of the eutectic phase initiates, leading to plastic flow at the grain boundaries. As the annealing temperature rises further to 1000 °C, this plastic flow intensifies, resulting in the formation of deep grooves in the microstructure. Consequently, the hardness and yield strength decrease rapidly, reaching 440 HV3 and 1437 MPa, respectively.

The high hardness value, as shown in Fig. 8, indicates that the alloy exhibits brittle deformation behavior.[22,38] For high entropy alloys with brittle behavior (containing significant proportions of BCC and IM phases), the yield strength (σ_y) and Vickers hardness (HV) are correlated by Tabor's relationship:[39]

$$\mathrm{YS} \cong \frac{\mathrm{HV}}{3}, \mathrm{MPa} \qquad (6)$$

The results of calculations based on this relationship for $FeCoNiAl_{0.75}Nb_{0.25}$ alloy are shown in Table 5. The compressive yield strength of the alloy is significantly higher than that of previously published alloys in the as-cast[23–25] and heat-treated state.[20,40] The replacement of elements (Cr, Mn, Cu and V) with Al and Nb, and the application of heat treatment significantly increased the hardness and strength of the alloy. The alloy densities calculated using HEAPS software for $FeCoNiAl_{0.75}Nb_{0.25}$, $FeCoNiCrNb_{0.25}$, FeCoNiCrMn, FeCoNiCrV, and $(FeCoNiCrMn)_{88}Nb_{12}$ are 7.45, 8.23, 8.06, 7.79, and 8.12 g cm^{-3}, respectively. The results indicate a reduction in density, which can help decrease the mass of the manufactured product while maintaining high hardness and strength.

The precipitation of multiple intermetallic phases in the microstructure did not enhance the magnetic properties of the alloy. In the as-cast state, the values for saturation magnetization (Ms) and coercivity (Hc) were 0.67 T and 716 A m^{-1},

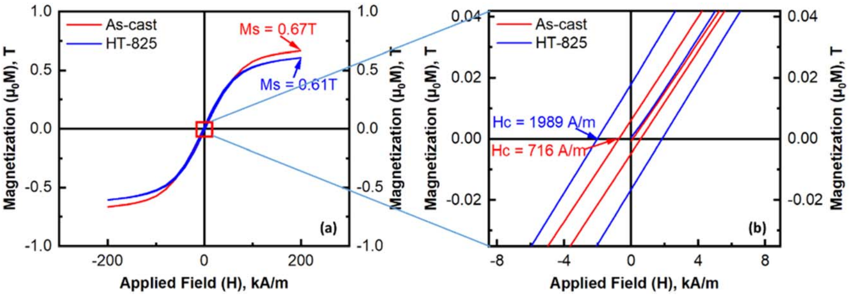

Fig. 9 Magnetization hysteresis loops: as-cast and HT-825 specimens.

Table 6 Compare magnetic properties of alloys

Alloys	Ms, emu g^{-1} (T)	Hc, Oe (A m^{-1})	Ref.
FeCoNiAl$_{0.75}$Nb$_{0.25}$ as-cast	68.00 (0.67)	9.00 (716)	This work
FeCoNiMnAl$_{0.7}$ as-cast	20.10 (0.19)	13.60 (1082)	Hariharan[41]
FeCoNiMnAl$_{0.75}$ as-cast	100.00 (0.93)	15.00 (1194)	Zuo *et al.*[42]
FeCoNiAlCrNb$_{0.25}$ as-cast	34.69 (0.31)	95.00 (7560)	Ma *et al.*[22]
FeCoNiAlCr as-cast	64.00 (0.57)	52.00 (4138)	Ma *et al.*[22]
FeCoNiAlCu as-cast	84.00 (0.79)	162 (12 892)	Kulkarni[43]
FeCoNiAl$_{0.65}$Mn$_{0.65}$ LMD	78.42 (0.74)	8.57 (699)	Bazioti[44]
FeCoNiAl$_{0.75}$Nb$_{0.25}$ HT-825	62.00 (0.61)	25.00 (1989)	This work
FeCoNiAl$_{0.75}$Mn HT-800	90.00 (0.83)	27.00 (2149)	Zuo *et al.*[42]

respectively. After heat treatment at 825 °C, these values changed to 0.61 *T* for saturation magnetization and 1989 A m^{-1} for coercivity, as shown in Fig. 9. These results indicate that the BCC phase in the as-cast microstructure is ferromagnetic and exhibits good soft magnetic properties. Although the phase at the grain boundary is abundant, up to 23%, it can consist of non-ferromagnetic or weakly ferromagnetic phases. Due to the rapid cooling during casting, Hc remains quite high within the grains. After annealing, even though the amount of precipitated phase increases, Ms decreases only slightly, by about 10%, suggesting the precipitation of weakly ferromagnetic or non-ferromagnetic phases. However, Hc increases significantly because these phases precipitate inside the grains. A comparative analysis with studies on alloys of similar compositions (Table 6) indicates that in the as-cast state, substituting a small amount of Mn with Nb enhances the saturation magnetization (Ms) while maintaining a relatively low coercivity (Hc) compared to the findings of Hariharan *et al.*[41] However, the Ms values remain considerably lower in both the as-cast and heat-treated states than those reported by Zuo *et al.*,[42] although the coercivity consistently remains lower. A similar trend is observed for the FeCoNiCu alloy.[43] This enhancement is slightly superior to that achieved by Cr addition in the FeCoNiAlCr alloy,[22] and significantly better than the FeCoNiAlCrNb$_{0.25}$ alloy.[22] Nonetheless, the magnetic properties of the alloy smelted in a vacuum induction furnace are almost equivalent to those of the Mn-containing alloy fabricated using the Laser Metal Deposition (LMD) method.

In as-cast state, the alloy demonstrates significant hardness and commendable magnetic properties. As a result, it highly suitable for use in magnetic parts that demand superior mechanical properties.

4. Conclusions

The influence of microstructure on the mechanical and magnetic properties of the FeCoNiAl$_{0.75}$Nb$_{0.25}$ high-entropy alloy after casting and heat treatment was studied. Changing the heat treatment temperature leads to changes in the phase characteristics of the alloy. The microstructure consists of a mixture of FCC, BCC, and IM phases however their proportions change after heat treatment. The precipitation in the BCC matrix starts at 755 °C and reaches a maximum at 825 °C, then decreases. In the as-cast state, the alloy demonstrates notable magnetic and mechanical properties, with hardness, compressive yield strength, saturation magnetization, and coercive force values of 493 HV, 1611 MPa, 0.67 T, and 716 A m^{-1}, respectively. Therefore, it is very suitable for use in magnetic parts requiring superior mechanical properties.

Data availability

The data supporting this article have been included as part of the ESI.†

Conflicts of interest

There are no conflicts to declare.

Acknowledgements

This research is funded by Le Quy Don Technical University Research Fund under the grant number 24.1.14.

References

1 J. W. Yeh, S. K. Chen, S. J. Lin, *et al.*, Nanostructured High-Entropy Alloys with Multiple Principal Elements: Novel Alloy Design Concepts and Outcomes, *Adv. Eng. Mater.*, 2004, **6**(5), 299–303.

2 J.-W. Yeh, S.-J. Lin, T.-S. Chin, *et al.*, Formation of simple crystal structures in Cu-Co-Ni-Cr-Al-Fe-Ti-V alloys with multiprincipal metallic elements, *Metall. Mater. Trans. A*, 2004, **35**(8), 2533–2536.

3 O. N. Senkov, G. B. Wilks, J. M. Scott and D. B. Miracle, Mechanical properties of Nb$_{25}$Mo$_{25}$Ta$_{25}$W$_{25}$ and V$_{20}$Nb$_{20}$Mo$_{20}$Ta$_{20}$W$_{20}$ refractory high entropy alloys, *Intermetallics*, 2011, **19**(5), 698–706.

4 O. N. Senkov, S. V. Senkova, D. B. Miracle and C. Woodward, Mechanical properties of low-density, refractory multi-principal element alloys of the Cr–Nb–Ti–V–Zr system, *Mater. Sci. Eng., A*, 2013, **565**, 51–62.

5 A. Gali and E. P. George, Tensile properties of high- and medium-entropy alloys, *Intermetallics*, 2013, **39**, 74–78.

6 F. Otto, A. Dlouhý, C. Somsen, H. Bei, G. Eggeler and E. P. George, The influences of temperature and microstructure on the tensile properties of a CoCrFeMnNi high-entropy alloy, *Acta Mater.*, 2013, **61**(15), 5743–5755.

7 A. V. Kuznetsov, D. G. Shaysultanov, N. D. Stepanov, G. A. Salishchev and O. N. Senkov, Tensile properties of an AlCrCuNiFeCo high-entropy alloy in as-cast and wrought conditions, *Mater. Sci. Eng., A*, 2012, **533**, 107–118.

8 A. V. Kuznetsov, D. G. Shaysultanov, N. Stepanov, G. Salishchev and O. Senkov, Superplasticity of AlCoCrCuFeNi high entropy alloy, *Mater. Sci. Forum*, 2013, **735**, 146–151.

9 C. Suryanarayana, Mechanical Alloying: A Novel Technique to Synthesize Advanced Materials, *Research*, 2019, 1–17.

10 M.-R. Chen, S.-J. Lin, J.-W. Yeh, M.-H. Chuang, P.-H. Lee and Y.-S. Huang, Effect of vanadium addition on the microstructure, hardness, and wear resistance of $Al_{0.5}$CoCrCuFeNi high-entropy alloy, *Metall. Mater. Trans. A*, 2006, **37**, 1363–1369.

11 Y. Wang, B. Li and H. Fu, Solid Solution or Intermetallics in a High-Entropy Alloy, *Adv. Eng. Mater.*, 2009, **11**, 641–644.

12 Y. L. Chou, J. W. Yeh and H. C. Shih, The effect of molybdenum on the corrosion behaviour of the high-entropy alloys $Co_{1.5}CrFeNi_{1.5}Ti_{0.5}Mo_x$ in aqueous environments, *Corros. Sci.*, 2010, **52**(8), 2571–2581.

13 M.-H. Chuang, M.-H. Tsai, W.-R. Wang, S.-J. Lin and J.-W. Yeh, Microstructure and wear behavior of $Al_xCo_{1.5}CrFeNi_{1.5}Ti_y$ high-entropy alloys, *Acta Mater.*, 2011, **59**(16), 6308–6317.

14 S. Singh, N. Wanderka, B. S. Murty, U. Glatzel and J. Banhart, Decomposition in multi-component AlCoCrCuFeNi high-entropy alloy, *Acta Mater.*, 2011, **59**(1), 182–190.

15 W.-R. Wang, W.-L. Wang, S.-C. Wang, Y.-C. Tsai, C.-H. Lai and J.-W. Yeh, Effects of Al addition on the microstructure and mechanical property of Al_xCoCrFeNi high-entropy alloys, *Intermetallics*, 2012, **26**, 44–51.

16 F. Otto, Y. Yang, H. Bei and E. P. George, Relative effects of enthalpy and entropy on the phase stability of equiatomic high-entropy alloys, *Acta Mater.*, 2013, **61**(7), 2628–2638.

17 D. G. Shaysultanov, N. Stepanov, A. V. Kuznetsov, G. Salishchev and O. Senkov, Phase Composition and Superplastic Behavior of a Wrought AlCoCrCuFeNi High-Entropy Alloy, *JOM*, 2013, **65**, 1815–1828.

18 J.-W. Yeh, Alloy Design Strategies and Future Trends in High-Entropy Alloys, *JOM*, 2013, **65**, 1759–1771.

19 J. Y. He, W. H. Liu, H. Wang, *et al.*, Effects of Al addition on structural evolution and tensile properties of the FeCoNiCrMn high-entropy alloy system, *Acta Mater.*, 2014, **62**, 105–113.

20 G. A. Salishchev, M. A. Tikhonovsky, D. G. Shaysultanov, *et al.*, Effect of Mn and V on structure and mechanical properties of high-entropy alloys based on CoCrFeNi system, *J. Alloys Compd.*, 2014, **591**, 11–21.

21 Y. Zhang, T. T. Zuo, Z. Tang, *et al.*, Microstructures and properties of high-entropy alloys, *Prog. Mater. Sci.*, 2014, **61**, 1–93.

22 S. G. Ma and Y. Zhang, Effect of Nb addition on the microstructure and properties of AlCoCrFeNi high-entropy alloy, *Mater. Sci. Eng., A*, 2012, **532**, 480–486.

23 N. Malatji, A. P. I. Popoola, T. Lengopeng and S. Pityana, Effect of Nb addition on the microstructural, mechanical and electrochemical characteristics of AlCrFeNiCu high-entropy alloy, *Int. J. Miner., Metall. Mater.*, 2020, **27**(10), 1332–1340.

24 G. Qin, Z. Li, R. Chen, *et al.*, CoCrFeMnNi high-entropy alloys reinforced with Laves phase by adding Nb and Ti elements, *J. Mater. Res.*, 2019, **34**(6), 1011–1020.

25 H. Jiang, L. Jiang, D. Qiao, *et al.*, Effect of niobium on microstructure and properties of the $CoCrFeNb_xNi$ high entropy alloys, *J. Mater. Sci. Technol.*, 2017, **33**(7), 712–717.

26 Y. Zhang, *High-entropy Materials: Advances and Applications*, 2023.

27 P. Li, A. Wang and C. T. Liu, Composition dependence of structure, physical and mechanical properties of $FeCoNi(MnAl)_x$ high entropy alloys, *Intermetallics*, 2017, **87**, 21–26.

28 X. Tan, Y. Tang, Y. Tan, *et al.*, Correlation between microstructure and soft magnetic parameters of Fe-Co-Ni-Al medium-entropy alloys with FCC phase and BCC phase, *Intermetallics*, 2020, **126**, 106898.

29 X. Yang and Y. Zhang, Prediction of high-entropy stabilized solid-solution in multi-component alloys, *Mater. Chem. Phys.*, 2012, **132**(2), 233–238.

30 M. G. Poletti and L. Battezzati, Electronic and thermodynamic criteria for the occurrence of high entropy alloys in metallic systems, *Acta Mater.*, 2014, **75**, 297–306.

31 A. Takeuchi and A. Inoue, Classification of Bulk Metallic Glasses by Atomic Size Difference, Heat of Mixing and Period of Constituent Elements and Its Application to Characterization of the Main Alloying Element, *Mater. Trans.*, 2005, **46**, 2817–2829.

32 S. Guo and C. T. Liu, Phase stability in high entropy alloys: Formation of solid-solution phase or amorphous phase, *Prog. Nat. Sci.:Mater. Int.*, 2011, **21**(6), 433–446.

33 M. Enoki and H. Ohtani, Relationship between Lattice Strain and Ordering Tendency in Medium-Entropy Alloys, *Mater. Trans.*, 2024, **65**(9), 1025–1033.

34 F. He, Z. Wang, P. Cheng, *et al.*, Designing eutectic high entropy alloys of CoCrFeNiNbx, *J. Alloys Compd.*, 2016, **656**, 284–289.

35 T. T. Zuo, R. B. Li, X. J. Ren and Y. Zhang, Effects of Al and Si addition on the structure and properties of CoFeNi equal atomic ratio alloy, *J. Magn. Magn. Mater.*, 2014, **371**, 60–68.

36 Z. Lei, X. Liu, Y. Wu, *et al.*, Enhanced strength and ductility in a high-entropy alloy via ordered oxygen complexes, *Nature*, 2018, **563**(7732), 546–550.

37 S. Chen, Z. H. Aitken, S. Pattamatta, *et al.*, Simultaneously enhancing the ultimate strength and ductility of high-entropy alloys via short-range ordering, *Nat. Commun.*, 2021, **12**(1), 4953.

38 N. Malatji, A. Popoola, T. Lengopeng, S. J. I. JoM. Pityana and M. Metallurgy, Effect of Nb addition on the microstructural, mechanical and electrochemical characteristics of AlCrFeNiCu high-entropy alloy, *Int. J. Miner., Metall. Mater.*, 2020, **27**, 1332–1340.

39 X. Fan, R. Qu and Z. Zhang, Relation Between Strength and Hardness of High-Entropy Alloys, *Acta Metall. Sin. (Engl. Lett.)*, 2021, **34**(11), 1461–1482.

40 C. Yang, J. Zhang, M. Li and X. J. A. M. S. Liu, Soft-magnetic high-entropy AlCoFeMnNi alloys with dual-phase microstructures induced by annealing, *Acta Metall. Sin. (Engl. Lett.)*, 2020, **33**, 1124–1134.

41 V. S. Hariharan, A. Karati, T. Parida, R. John, D. Babu and B. Murty, Effect of Al addition and homogenization treatment on the magnetic properties of CoFeMnNi high-entropy alloy, *J. Mater. Sci.*, 2020, **55**, 1–14.

42 T. Zuo, Y. Cheng, P. Chen, Z. Gao, Y. Zhang and P. K. Liaw, Structural and magnetic transitions of CoFeMnNiAl high-entropy alloys caused by composition and annealing, *Intermetallics*, 2021, **137**, 107298.

43 R. Kulkarni, B. S. Murty and V. Srinivas, Study of microstructure and magnetic properties of AlNiCo(CuFe) high entropy alloy, *J. Alloys Compd.*, 2018, **746**, 194–199.

44 C. Bazioti, O. M. Løvvik, A. Poulia, *et al.*, Probing the structural evolution and its impact on magnetic properties of FeCoNi$(AlMn)_x$ high-entropy alloy at the nanoscale, *J. Alloys Compd.*, 2022, **910**, 164724.